# Temporal Evolution of Flux Tube Entanglement at the Magnetopause as Observed by the MMS Satellites

**Y. Qi[1], C.T. Russell[1], Yingdong Jia[1], M. Hubbert[1]**

[1]Earth Planetary and Space Sciences, University of California Los Angeles, Los Angeles, CA 90095-1567.

Corresponding author: Yi Qi (yqi@ucla.edu)

**Key Points:**

- 17 entanglement events are identified.
- Entanglement occurs more often under By-dominated IMF.
- Entanglement evolves in three distinguishable stages

**Abstract**

Flux transfer events (FTEs), as flux ropes (FRs), are considered key agents for solar wind energy to enter the terrestrial magnetosphere. Recent observations identify entangled flux tubes that collide and pull against each other. Reconnection occurs to disentangle and produce a new pair of flux ropes with different connectivity. In this paper, we examine how such an entanglement process evolve in time by comparing 17 entanglements observed by the Magnetospheric Multiscale (MMS) mission. The $B_y$-dominated interplanetary magnetic field (IMF) distribution of the entangled tubes agrees with previous findings. We have identified three evolutionary stages characterized by the magnetic field and pressure enhancement. Our study confirms the flux rope nature of these events and explains how a disparate pair of ropes is formed from two entangled flux tubes, each initially connected to a different hemisphere of the magnetosphere.

**Plain Language Summary**

The Earth's intrinsic magnetic field deflects the solar wind flow at a boundary called the magnetopause. Near this boundary, twisted flux tubes are found when the external field in the solar wind is southward. Such tubes may become entangled if they move towards each other, say from the southern and northern hemispheres. This study analyzes 17 events like this and identifies three evolutionary stages as the entanglement proceeds. The results improve our understanding of not only the complex coupling between solar wind and the Earth's magnetic field, but other similar processes in space plasma.

## 1 Introduction

Flux transfer events (FTEs) were first observed by the ISEE 1 and 2 spacecraft and were interpreted as generated by patchy and impulsive reconnection near the sub-solar point (Russell & Elphic, 1979). Following the first discovery, other generation models were raised, including the multiple X-line model by Lee & Fu (1985), and a single X-line model with a time-varying reconnection rate (Scholer, 1988; Southwood et al., 1988). The different generation mechanisms may be associated with different upstream conditions and could result in different magnetic field topology and connectivity within/around the FTE (Dorelli & Bhattacharjee, 2009; Hesse et al., 1990; Hwang et al., 2020; Pu et al., 2013). Despite differences in detail, all models agree that reconnection plays an essential role in transferring magnetic flux. The most notable yet simple feature of an FTE common to the various models is enhanced magnetic field strength, with a bipolar $B_N$ component in boundary normal coordinates, indicating that the magnetic field is twisted like a rope.

Reconnection can happen at multiple locations simultaneously at the magnetopause; Thus the motion of the flux tubes leaving reconnection sites may become intricate, especially when the interplanetary magnetic field (IMF) has a large By component (Fargette et al., 2020; Kan, 1988; Nishida, 1989; Otto, 1991; Zhao, 2019). Two flux tubes, with one end connected to the northern/ southern hemisphere of the Earth and the other end connected to the magnetosheath, that flow away from their original reconnection sites may collide and become entangled. The magnetic field becomes highly compressed around the interface of these two entangled flux tubes.

Secondary reconnection can occur within the flux pile-up region and alter the field line connectivity. Previous three-dimensional MHD simulations (Fedder et al., 2002; Lee et al., 1993), global hybrid simulations (Tan et al., 2011) and observations (Bogdanova et al., 2008; Lv et al., 2016; Pu et al., 2013) have examined how reconnection enables the field topology changes, and have shown four resulting magnetic field bundle topologies: one end connected to the magnetosheath and the other end to the Earth's northern/southern hemisphere; both ends connected to the magnetosphere; and both ends connected to the magnetosheath.

Recently, with the improvement of spatial and temporal resolution of instruments, direct observations of flux tube entanglement/interlinked flux tubes (Fargette et al., 2020; Hwang, Dokgo et al., 2020; Kacem et al., 2018; Kieokaew & Foullon, 2019; Øieroset et al., 2019) were reported. These studies pointed out the differences between a classic flux rope and two entangled/interlinked flux tubes: a significant pressure enhancement which violates the force-balanced flux rope model (Russell et al., 2017); a sharp rotation of magnetic field at the field strength peak region instead of a smooth bipolar variation in the transverse direction; and disparate plasma on two sides of this thin current indicating the lack of magnetic connectivity. In these studies, reconnection characteristics have been carefully identified at the entanglement interface. As it proceeds, reconnection is expected to resolve the entanglement and generate a new pair of flux ropes. In contrast to the initial pair which has one end connected to Earth and the other to the sheath, now one rope has both ends connected in the magnetosheath while the other one has both ends connected in the magnetosphere (Russell & Qi, 2020).

The purpose of this study is to investigate the temporal evolution of flux tube entanglement, and further evaluate the impact of the reconnection between entangled flux tubes. We examined 17 entanglement events. We identify the characteristics of entanglement at different stages using their differences and similarities in the field line geometry, the pressure profile, and electron distributions. Section 2 introduces the instruments and datasets used in this study. In section 3 we use three representative events to outline the three evolutionary stages of flux rope entanglement. Then we revisit a classic entanglement event with additional analysis at the interface and give a full list of the 17 selected events. Then, based on three representative events, the temporal evolution stages are elaborated. Section 4 includes further discussions and a summary of our findings.

## 2 Data and Methodology

All flux tube entanglement events studied here are observed by the Magnetospheric Multiscale (MMS) mission (Burch et al., 2015) during its first two dayside phases (Winter 2015-2016 and Winter 2016-2017) (Fuselier et al., 2016). During these time periods, at the magnetopause, the MMS maintains a tetrahedron formation at apogee with spacecraft separation usually below 100 km, which allows us to analyze spatial gradients close to the electron-kinetic scale. The magnetic field is measured by the fluxgate magnetometer (FGM) (Russell et al., 2014) at its highest sampling rate of 128 Hz. Fast plasma investigation (FPI) instruments (Pollock et al., 2016) provide the electron/ion distribution functions and moments every 30/150 ms at burst mode, covering the energy range from 10 eV to 30 keV. Solar wind conditions are examined for each event using measurements from the OMNI database (King & Papitashvili, 2005).

## 3 Observations

3.1 Selecting entanglement cases

Based on the previous case studies mentioned in the introduction section (Fargette et al., 2020; Hwang, Dokgo, et al., 2020; Kacem et al., 2018; Kieokaew & Foullon, 2019; Øieroset et al., 2019), we used the following criteria to identify the flux tube entanglement:

- A significant increase in both magnetic field strength and total pressure (the sum of plasma thermal $nkT$ pressure and magnetic pressure $B^2/(2\mu¿¿0)¿$)
- A sharp rotation of the magnetic field (i.e., a thin current sheet) around the maximum pressure location
- A sudden change in the electron pitch-angle distribution across the central current sheet

| No. | Date | Start time | End time | Location (GSM) [RE] | Delta P [%] | Notes |
|---|---|---|---|---|---|---|
| 1 | 2016-12-10 | 04:52:59 | 04:54:04 | [9.55, 0.14, -0.46] | 59 | 1 |
| 2 | 2015-10-31 | 07:17:44 | 07:19:06 | [10.73, 3.48, -2.31] | 73 | 1 |
| 3 | 2015-11-07 | 14:16:22 | 14:16:55 | [8.62, 5.42, -3.22] | 160 | 1 |
| 4* | 2017-05-05 | 20:06:42 | 20:06:57 | [-13.97, -17.91, -4.76] | 139 | 2 |
| 5 | 2015-11-05 | 14:47:06 | 14:47:34 | [8.17, 5.74, -3.27] | 83 | 3 |
| 6 | 2015-11-21 | 01:55:59 | 01:57:38 | [9.73, -1.42, -0.35] | 112 | 3 |
| 7 | 2016-02-10 | 02:47:23 | 02:48:14 | [6.45, -7.68, -4.61] | 28 | 3 |
| 8 | 2016-12-28 | 04:59:12 | 04:59:46 | [10.9, -1.6, 0.1] | 94 | 3 |
| 9 | 2015-12-08 | 10:27:41 | 10:28:07 | [10.81, 0.82, -1.27] | 46 | 3 |
| 10 | 2016-02-26 | 01:48:54 | 01:49:11 | [4.28, -7.91, -5.48] | 99 | 3 |
| 11 | 2016-11-12 | 17:50:27 | 17:51:25 | [6.6, 9.17, -1.09] | 121 | 3 |
| 12 | 2015-11-06 | 13:23:31 | 13:24:24 | [9.27, 5.26, -3.38] | 212 | 4 |
| 13 | 2015-12-03 | 10:24:08 | 10:25:13 | [11.04, 1.31, -1.48] | 60 | 4 |
| 14 | 2016-01-18 | 01:22:46 | 01:23:11 | [8.57, -7.43, -3.92] | 49 | 4 |
| 15 | 2015-10-11 | 12:48:52 | 12:49:31 | [8.01, 7.35, -5.06] | 69 | 4 |
| 16 | 2015-11-17 | 14:20:56 | 14:21:05 | [8.48, 4.48, -2.52] | 97 | 4 |
| 17 | 2015-11-17 | 14:21:45 | 14:21:59 | [8.48, 4.48, -2.52] | 83 | 4 |

**Table 1.** The time and location of the identified flux tube entanglement events. As labeled in the notes column, some events have been reported in recent publications: 1. (Øieroset et al., 2019); 2. (Hwang, Dokgo, et al., 2020); 3. (Fargette et al., 2020); 4. This paper. Event 4 has been studied as entanglement between flux tubes generated within a Kelvin-Helmholtz vortex, but is not detected at the dayside magnetopause.

Table 1 lists all the events with their times and locations in the Geocentric Solar Magnetospheric (GSM) coordinate system. Event location is slightly biased towards the dusk side, with 10 of 17 events located in positive Y GSM (Fig. 1b). Events also tend to appear below the equator in a limited Z_GSM range (< 6 $R_E$), which may be caused by the longer dwell time of the MMS in the southern hemisphere and the limited latitude coverage of the orbits. In general, the entanglement events are ubiquitous and suggesting that flux tube entanglement happens frequently at the magnetopause. Figure 1a shows the solar wind clock angle of these events. In contrast with the finding that reconnection is favored by antiparallel fields, FTEs generated by these twisted flux tubes and their entanglement are favored by a By-dominated IMF condition. This agrees with earlier findings of Fargette et al. (2020) and Russell & Qi (2020).

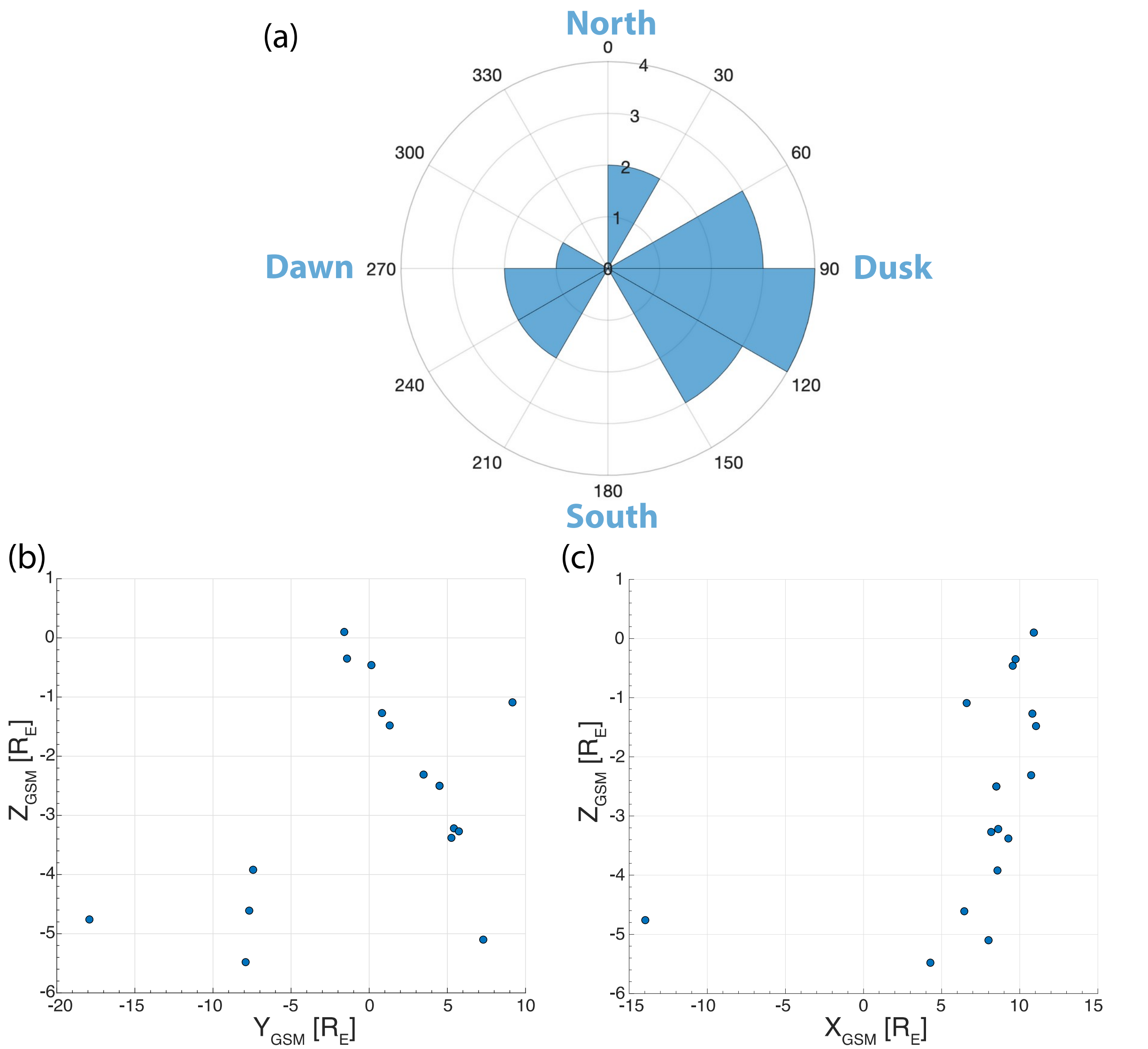


**Figure 1**. IMF conditions and locations of 17 events. **(a)** Solar wind clock angle measured by the MMS during the 17 events. Starting from 0°, each bin is 30° wide. The bar length in units of radius is the number of events in that clock angle bin. **(b), (c)** The locations of 17 events in the GSM Y-Z and X-Z planes. Event 4 has been studied as entanglement between flux tubes generated within a Kelvin-Helmholtz vortex, but is not detected at the dayside magnetopause

3.2 Three stages of entanglement

Before introducing the temporal evolutionary features in the MMS data, we qualitatively describe the entanglement process and the expected characteristics of its different temporal evolutionart stages. As shown in the sketch of Russell & Qi, 2020, two flux tubes generated at different primary reconnection sites moves towards each other. These tubes have one end connected to the Earth, and the other end connected to the magnetosheath. When the two flux tubes encounter each other, there is no way for them to pass. Instead they become entangled and stretched, with significantly enhanced compression at the interface. How do they eventually disentangle? We have identified three typical cases to examine this evolution process.

Figure 2 compares three typical events to show the temporal evolution of flux tube entanglement: event no. 13 (left), event no. 3 (middle), and event no. 1 (right) in Table 1. We rotate the data into an LMN coordinate system, i.e., for event 3 in the middle panels, N is the current sheet normal direction determined by four-spacecraft timing, M' is the averaged current direction (current interval is marked by blue vertical lines in figure 2), L direction is perpendicular to the plane containing both N and M', and finally $N \times L$ gives the M. For each event, we show the four-spacecraft-averaged magnetic field, the current density, the pressure, and the ion and electron energy spectrogram observed by MMS1 in a wider time range to demonstrate the full entanglement (pressure enhancement) region as marked by the black vertical lines. The magnetic field curvature projected in the current sheet moving (normal) direction is plotted in a narrower time interval marked by the blue vertical lines and centered around the current sheet. The red vertical line marks the maximum current density location within the current sheet.

In the top panels which correspond to the early stage (event no. 13), the curvature normal component varies around zero, showing no systematic pattern at the central current sheet. The total pressure enhancement is only about 60% of its ambient value, indicating a not-yet-grown compression as the two flux tubes just start to interact. Throughout the entire pressure enhanced region in event no.13, the MMS does not observe a significant electron population at energies above 1keV. This is consistent with an early stage of entanglement, when neither of the two entangled flux tube are "closed" in the magnetosphere. Thus it is difficult for them to trap the hot magnetopsheric electrons.

As the entanglement proceeds, the field lines bend more toward the current sheet, keep adding magnetic tension force, leading to further increased compression. The most outstanding difference between event no. 3 (middle panels) and the other two is the curvature normal component. The clear negative-to-positive bipolar signature of the curvature normal in event no. 3 indicates that the magnetic field lines are curving towards the central current sheet on both sides. Magnetic flux piles up around the central current sheet, knocking the total pressure off balance (middle pressure panel of Figure 2, or enlarged plot in Figure 3d), and preparing for a secondary reconnection to release the energy (Øieroset et al., 2019). The total pressure enhancement is about 190% of the ambient value. These features are consistent with this being the stage when the two flux tubes are actively pulling against each other, and the magnetic field wraps around the interface tightly. Noting the strong pressure build-up and the negative-to-positive bipolar curvature N component, we label event no. 3 as the middle stage of the entanglement process.

Eventually, a new pair of ropes are about to be born, as shown in the bottom panels (event no. 1). In contrast with the initial pair, one rope has both ends connected to the ionosphere ("closed" in the magnetosphere) while the other rope has two ends connected to the magnetosheath ("interplanetary"). The "closed" flux rope is capable of trapping energetic magnetospheric electrons. The "interplanetary" flux rope will lose its energetic electrons quickly. Comparable to the early stage event no. 13, the curvature normal component remains insignificant except in the current sheet region in event no. 1. The total pressure enhancement is

70% in event no. 1, similar to that of the entanglement in its early stage. At this late stage, the compression has been canceled when reconnection has almost released the entanglement and the new ropes are about to form. The key difference between event no. 13 and event no. 1 is in the electron distributions. In event no. 1, the right half of the pressure enhanced region shows increased flux between 1k – 10 keV, which is absent in the left half. This is consistent with a later stage of entanglement when reconnection has almost finished making two new ropes one of which (like the right half in event no. 13) has the majority of its field lines connected to the southern and northern hemisphere of the Earth and is capable of trapping the hot electrons originating from the plasma sheet.

As sketched on right of each event in Figure 2, based the events we identified (in Table 2), we summarize the temporal evolution characteristics of flux tube entanglement as follows:

- The three most diagnostic parameters to examine are: 1) the total pressure; 2) the curvature component along the current sheet normal; and 3) the hot electron flux.
- An early-stage entanglement does not have the bipolar variation in curvature and has less significant pressure enhancement (< 100%), indicating the two flux tubes are loosely compressed. There are no clear energetic magnetospheric electron flux increases on either side because the flux tubes have not been sufficiently "closed" in the magnetosphere, thus it is harder for them to trap hot electrons.
- A mid-stage entanglement exhibits a clear bipolar curvature normal component, and a fairly strong total pressure increase (> 100%), indicating the significant compression between two tubes. A hot electron population may or may not be present due to the co-existence of magnetic field lines with different connectivity.
- A late-stage entanglement does not have the bipolar variation in curvature and has less significant pressure enhancement (< 100%), as the compression has mostly resolved by reconnection. Energetic magnetospheric electrons appear either before or after the current sheet crossing, indicating that the field lines on this side are almost "closed" (i.e., have two ends on the Earth), and a new pair of flux ropes is about to be born.

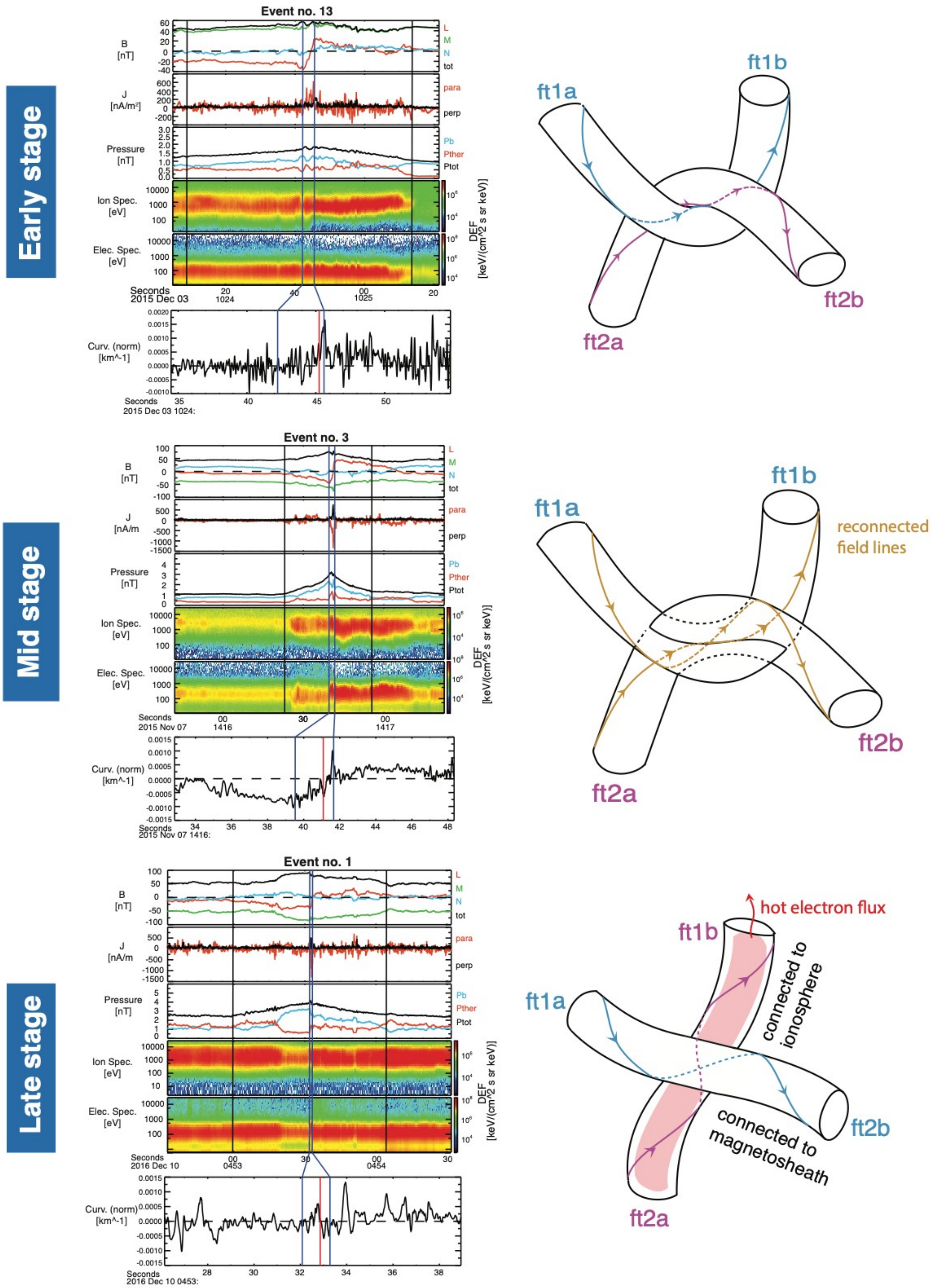
Early stage
Event no. 13
ft1a
ft1b
ft2a
ft2b
Mid stage
Event no. 3
ft1a
ft1b
ft2a
ft2b
reconnected field lines
Late stage
Event no. 1
hot electron flux
ft1a
ft1b
ft2a
ft2b
connected to ionosphere
connected to magnetosheath

215

**Figure 2**. Context plot for three representative events and schematic sketches showing characteristics of early, mid and late stages of the entanglement. We show the four-spacecraft-averaged magnetic field, the current density, the pressure, the ion and electron energy spectrogram in a wider time range to demonstrate the full entanglement (pressure enhanced) region as marked by the black vertical lines. The magnetic field curvature projected in the direction of the current sheet normal is plotted in a narrower time interval around the sheet marked by the blue vertical lines. The red vertical line marks the maximum current density location within the current sheet. The LMN rotation matrix for event no. 3 has been mentioned in the text. The LMN directions in GSM for event no. 13 are L: [0.50, -0.86, -0.06], M: [0.42, 0.18, 0.89], N: [0.75, 0.47, -0.46] , for event no.3 are L: [-0.08, -0.92, 0.39], M: [-0.78, -0.19, -0.59], N: [-0.62, 0.36, 0.70], and for event no. 1 are L: [0.66, -0.58, -0.48], M: [-0.34, 0.34, -0.88], N: [-0.67, -0.74, -0.03].

We use the mid stage event, event no.3 (November 7, 2015) as an example for further analysis of the highly compressed interface between two entangled flux tubes The sharp rotation of the magnetic field is clearly seen as the $B_L$ reversal from 14:16:39.527 to14:16:41.660. $B_N$ is close to zero. $B_M$ remains strong and enhanced at the current density peak time (indicated by the red vertical line). The current density dramatically increased around the maximum magnetic flux pile-up region. The dominant component of current is anti-parallel to the magnetic field and the magnitude reaches over 1000 nA/m$^2$. The normal speed of this current sheet is about 90 km/s. With a timespan of 2.1 seconds (between the blue vertical lines), the current sheet thickness is ~190 km. Electron bulk flow velocity increases significantly in the current sheet and deviates from the ion bulk flow velocity, especially in the M direction, suggesting that the current is mainly carried by the electrons. The electron flow accelerates and reverses in the L direction (Fig. 2e). Meanwhile, the ion flow increases in the -L direction (Fig. 2f), consistent with the current sheet actively reconnecting. Fig. 2h-l manifests the abrupt change in the energy spectra (Fig. 2h, i), as well as the electron pitch-angle distribution (Fig. 2j-l). Last, in panel (d), the curvature of magnetic field increased around the current sheet, plus a clear bipolar signature: it is negative before the MMS encounters the current sheet and reverses to positive after crossing the current sheet, indicating that the field lines bend towards the current sheet on both sides. This is consistent with the compression of the magnetic field, providing magnetic tension force to balance the pressure. Also consistently, in Fig. 2g, the green line is the estimated total pressure including the curvature force in the normal direction integrated along the path away from the current sheet center/maximum current density location ( $P_{curv} = \int \frac{B^2}{\mu_0} \left| Curv_N \right| dx = \int \frac{B^2}{\mu_0} \left( \overline{curv} \cdot \overrightarrow{V_{i,perp}} \right) dt$, where B is the magnetic field strength, $\mu_0$ is the vacuum permeability, $Curv_N$ is the curvature normal component, $\overrightarrow{V_{i,perp}}$ is the ion bulk flow velocity perpendicular to the magnetic field). This modified total pressure (green line in Fig. 2g) on the right appears stable, but on the left, there still remains an apparent slope, suggesting pressure balance has not yet been reached during such a dynamic process.

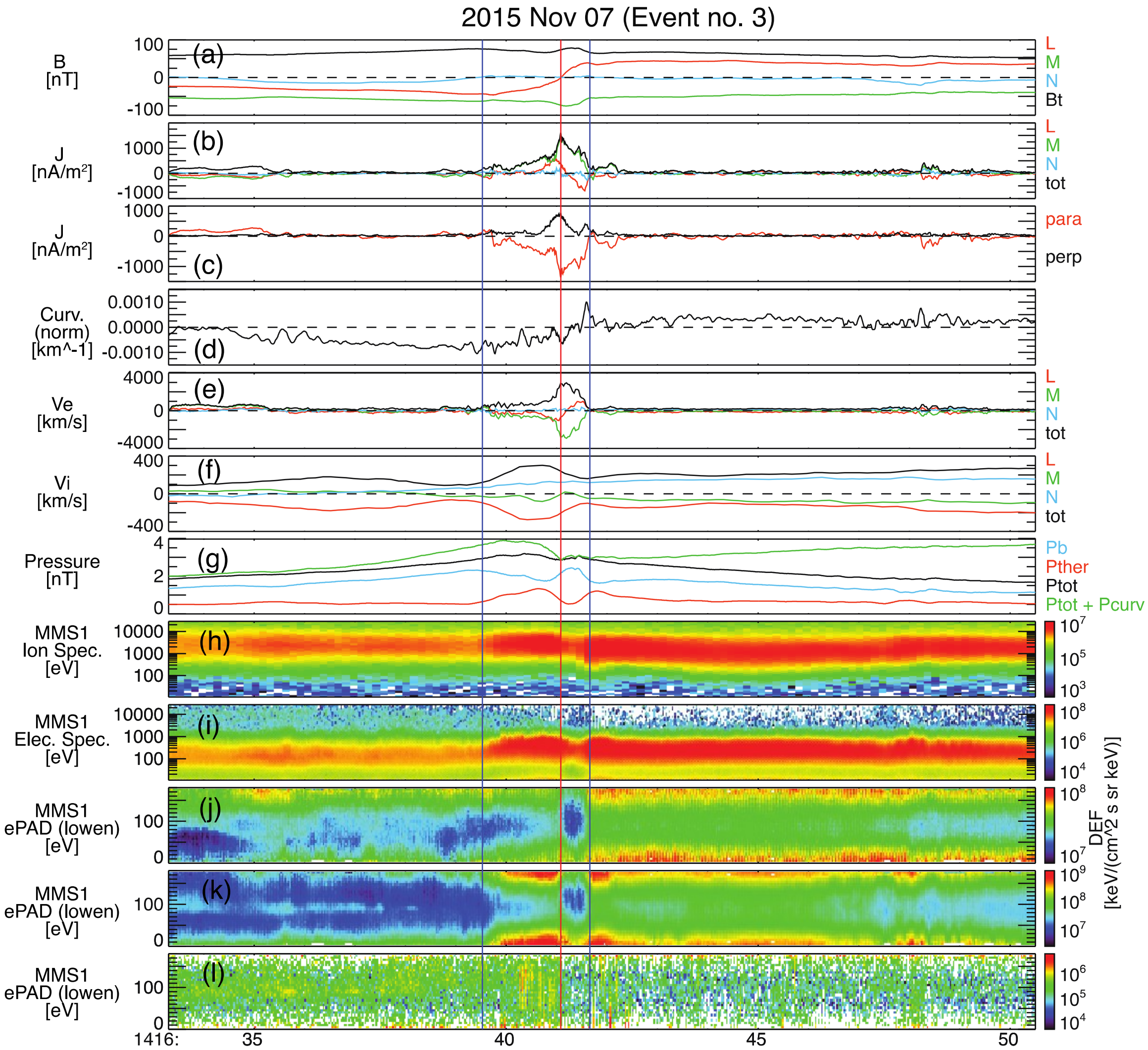


**Figure 3**. An example of two entangled flux tubes as observed by the MMS on 2015 November 7. **(a)** Four-spacecraft-averaged magnetic field in LMN coordinates and the field strength; **(b), (c)** current density computed by curlometer technique in LMN and field-aligned coordinates; **(d)** magnetic field curvature projected in the direction of central current sheet normal; **(e), (f)** four-spacecraft-averaged electron and ion bulk flow velocity; **(g)** four-spacecraft-averaged pressure; **(h), (i)** ion and electron energy spectrogram at MMS1; **(j)-(l)** electron pitch-angle distribution for low (10eV-200 eV), mid (200eV-2 keV), and high (2 keV-30 keV) energy range at MMS1. Blue vertical lines mark the central current sheet between two entangled flux tubes. The red vertical line marks the location of strongest current density within this current sheet.

## 4 Discussion and Conclusions

We applied the criteria outlined in the previous section to all 17 events, and we have classified 2 events as early-stage (nos. 9 and 13), 3 events as mid-stage (nos. 3, 6 and 11), and 3 events as late-stage (nos. 1, 8 and 13). The other events are ambiguous and cannot easily be classified into any of the three stages, due to the mixture of characteristics. The rest events show fewer diagnostic features. This is to be expected since the entanglement is a continuously developing process, and we do not expect a clear boundary between different stages. For example, in event no. 11 (Figure 1 in supplementary material), the total pressure enhancement is greater than 100% of the ambient plasma, and to the left of the central current sheet, the curvature normal component becomes negative, however, to the right of the central current sheet, there is no clear positive curvature normal component, thus the lack of bipolar signature but a relatively strong compression indicates event no. 11 is in a transition stage either between early and middle, or between middle and late. Another example is event no. 2 (Figure 2 in supplementary material). While there exists the bipolar signature in the curvature, the pressure enhancement is not as strong as other mid-stage events, thus it also seems to be in a transition stage.

To further examine if the properties of the current sheet between two entangled flux tubes are able to reveal the temporal evolution, we list additional information about these local current sheets for each of the eight events in Table 1 of the supplementary material. The duration of the entanglement events (the timespan between the event start time and the end time listed in Table 1) has a wide range from ~30 seconds to ~100 seconds, suggesting that the spatial scale of entanglement varies. The magnitude of entanglement depends on the sizes of the flux tubes, which is determined by the primary reconnection rate and duration. The velocity of the central current sheet is relatively slow, as to be expected in two tubes tugging in opposite directions. Except in event no. 9, current sheets in the rest of the events move at a speed close to or below 100 km/s. The current sheet duration is manually determined as the timespan of the magnetic field rotation region around the pressure peak. The current sheet width is computed by normal speed multiplied by the current sheet duration. There are two events (no. 1 and no. 13) with thin current sheets (close to or smaller than ion inertial length). Other current sheets are thicker, but still thinner than 5 ion inertial lengths. The current sheet ratio, computed as the timespan of the current sheet divided by the timespan of the event duration, is below 7%. This parameter quantitatively describes how "sharp" the field rotation is at the center, and this sharp rotation certainly differs from a smooth variation, as seen in an isolated stable flux rope. None of these parameters are informative about the temporal development sequences. This implies that flux tube entanglement may happen under varying conditions, like varying flux tube sizes, and/or plasma flow speed.

The total pressure profile in event no. 3 is very symmetric, as are most events. However, 5 out of 17 events are asymmetric (event nos. 7, 10, 11, 12 and 14). This asymmetry may be due to the differences in size and momentum of the two flux tubes. They do not occur as often as symmetric ones. One possible explanation is, if one tube is significantly weaker than another tube, it will easily be overpowered or merged. Under this circumstance, the entanglement process would not last as long, and would be observed less frequently.

In this study, we examined a list of 17 flux tube entanglement events from the first two dayside phases of the MMS observations. Their $B_y$-dominated IMF distribution agrees with previous findings. By comparing their similarities and differences in the magnetic field curvature, total pressure, and existence of hot electrons, we select eight events to showcase the temporal evolutionary features of three stages. They show that mid-stage entanglement events usually have the clearest bipolar signature in the curvature normal component, and a fairly strong total pressure increase (> 100%). Early-stage and late-stage entanglement does not have the bipolar variation in curvature and has less significant pressure enhancement (<100%). In late-stage events, energetic magnetospheric electrons appear either before or after the central current sheet crossing, indicating that one set of field lines is almost closed (having two ends on the Earth), and a new pair of flux ropes is about to be born.


## Acknowledgments

This research was supported by the NASA Magnetospheric Multiscale Mission, in association with NASA contract NNG04EB99C. The work at UCLA was supported through subcontract 06-001 with the University of New Hampshire. We thank the many individuals who operate the spacecraft and instruments and ensure the data are accurate and are provided to the science team in a timely manner. We would also like to thank Dr. San Lu for very beneficial discussions.


## Data Availability Statement

MMS data are available publicly from the mission's Science Data Center (https://lasp.colorado.edu/mms/sdc/public/). Solar wind data is available at CDAWeb (https://cdaweb.sci.gsfc.nasa.gov).

## References


Bogdanova, Y. V., Owen, C. J., Dunlop, M. W., Wild, J. A., Davies, J. A., Lahiff, A. D., et al. (2008), Formation of the low-latitude boundary layer and cusp under the northward IMF: Simultaneous observations by Cluster and Double Star: LLBL AND CUSP UNDER NORTHWARD IMF. *Journal of Geophysical Research: Space Physics*, *113*(A7). https://doi.org/10.1029/2007ja012762

Burch, J. L., Moore, T. E., Torbert, R. B., & Giles, B. L. (2015), Magnetospheric Multiscale Overview and Science Objectives. *Space Science Reviews*, *199*(1–4), 5–21. https://doi.org/10.1007/s11214-015-0164-9

Dorelli, J. C., & Bhattacharjee, A. (2009), On the generation and topology of flux transfer events. *Journal of Geophysical Research: Space Physics (1978–2012)*, *114*(A6). https://doi.org/10.1029/2008ja013410

Fargette, N., Lavraud, B., Øieroset, M., Phan, T. D., Toledo-Redondo, S., Kieokaew, R., et al. (2020), On the ubiquity of magnetic reconnection inside flux transfer event-like structures at the Earth's magnetopause. *Geophysical Research Letters*. https://doi.org/10.1029/2019gl086726

Fedder, J. A., Slinker, S. P., Lyon, J. G., & Russell, C. T. (2002), Flux transfer events in global numerical simulations of the magnetosphere. *Journal of Geophysical Research: Space Physics (1978–2012)*, *107*(A5), SMP 1-1-SMP 1-10. https://doi.org/10.1029/2001ja000025

Fuselier, S. A., Lewis, W. S., Schiff, C., Ergun, R., Burch, J. L., Petrinec, S. M., & Trattner, K. J. (2016), Magnetospheric Multiscale Science Mission Profile and Operations. *Space Science Reviews*, *199*(1–4), 77–103. https://doi.org/10.1007/s11214-014-0087-x

Hesse, M., Birn, J., & Schindler, K. (1990), On the topology of flux transfer events. *Journal of Geophysical Research*, *95*(A5), 6549. https://doi.org/10.1029/ja095ia05p06549

Hwang, K.-J, Dokgo, K., Choi, E., Burch, J. L., Sibeck, D. G., Giles, B. L., et al. (2020), Magnetic Reconnection Inside a Flux Rope Induced by Kelvin-Helmholtz Vortices. *Journal of Geophysical Research: Space Physics*, *125*(4). https://doi.org/10.1029/2019ja027665

Hwang, K.-J, Nishimura, Y., Coster, A. J., Gillies, R. G., Fear, R. C., Fuselier, S. A., et al. (2020), Sequential Observations of Flux Transfer Events, Poleward-Moving Auroral Forms, and Polar Cap Patches. *Journal of Geophysical Research: Space Physics*, *125*(6). https://doi.org/10.1029/2019ja027674

Kacem, I., Jacquey, C., Génot, V., Lavraud, B., Vernisse, Y., Marchaudon, A., et al. (2018), Magnetic Reconnection at a Thin Current Sheet Separating Two Interlaced Flux Tubes at the Earth's Magnetopause. *Journal of Geophysical Research: Space Physics*, *123*(3), 1779–1793. https://doi.org/10.1002/2017ja024537

Kan, J. R. (1988), A theory of patchy and intermittent reconnections for magnetospheric flux transfer events. *Journal of Geophysical Research*, *93*(A6), 5613. https://doi.org/10.1029/ja093ia06p05613

Kieokaew, R., & Foullon, C. (2019), Kelvin-Helmholtz Waves Magnetic Curvature and Vorticity: Four-Spacecraft Cluster Observations. *Journal of Geophysical Research: Space Physics*, *124*(5), 3347–3359. https://doi.org/10.1029/2019ja026484

King, J. H., & Papitashvili, N. E. (2005), Solar wind spatial scales in and comparisons of hourly Wind and ACE plasma and magnetic field data. *Journal of Geophysical Research*, *110*(A2). https://doi.org/10.1029/2004ja010649

Lee, L. C., & Fu, Z. F. (1985), A theory of magnetic flux transfer at the Earth's magnetopause. *Geophysical Research Letters*, *12*(2), 105–108. https://doi.org/10.1029/gl012i002p00105

Lee, L. C., Ma, Z. W., Fu, Z. F., & Otto, A. (1993), Topology of magnetic flux ropes and formation of fossil flux transfer events and boundary layer plasmas. *Journal of Geophysical Research: Space Physics*, *98*(A3), 3943–3951. https://doi.org/10.1029/92ja02203

Lv, L., Pu, Z., & Xie, L. (2016), Multiple magnetic topologies in flux transfer events: THEMIS measurements. *Science China Technological Sciences*, *59*(8), 1283–1293. https://doi.org/10.1007/s11431-016-6071-9

Nishida, A. (1989), Can random reconnection on the magnetopause produce the low latitude boundary layer? *Geophysical Research Letters*, *16*(3), 227–230. https://doi.org/10.1029/gl016i003p00227

Øieroset, M., Phan, T. D., Drake, J. F., Eastwood, J. P., Fuselier, S. A., Strangeway, R. J., et al. (2019), Reconnection With Magnetic Flux Pileup at the Interface of Converging Jets at the Magnetopause. *Geophysical Research Letters*, *46*(4), 1937–1946. https://doi.org/10.1029/2018gl080994

Otto, A. (1991), Three-dimensional magnetohydrodynamic simulations of processes at the earth's magnetopause. *Geophysical & Astrophysical Fluid Dynamics*, *62*(1–4), 69–82. https://doi.org/10.1080/03091929108229126

Pollock, C., Moore, T., Jacques, A., Burch, J., Gliese, U., Saito, Y., et al. (2016), Fast Plasma Investigation for Magnetospheric Multiscale. *Space Science Reviews*, *199*(1–4), 331–406. https://doi.org/10.1007/s11214-016-0245-4

Pu, Z. Y., Raeder, J., Zhong, J., Bogdanova, Y. V., Dunlop, M., Xiao, C. J., et al. (2013), Magnetic topologies of an in vivo FTE observed by Double Star/TC-1 at Earth's magnetopause. *Geophysical Research Letters*, *40*(14), 3502–3506. https://doi.org/10.1002/grl.50714

Russell, C. T., & Elphic, R. C. (1979), ISEE observations of flux transfer events at the dayside magnetopause. *Geophysical Research Letters*, *6*(1), 33–36. https://doi.org/10.1029/gl006i001p00033

Russell, C. T., & Qi, Y. (2020), Flux Ropes Are Born in Pairs: An Outcome of Interlinked, Reconnecting Flux Tubes. *Geophysical Research Letters*. https://doi.org/10.1029/2020gl087620

Russell, C. T., Anderson, B. J., Baumjohann, W., Bromund, K. R., Dearborn, D., Fischer, D., et al. (2014), The Magnetospheric Multiscale Magnetometers. *Space Science Reviews*, *199*(1–4), 189–256. https://doi.org/10.1007/s11214-014-0057-3

Russell, C. T., Strangeway, R. J., Zhao, C., Anderson, B. J., Baumjohann, W., Bromund, K. R., et al. (2017), Structure, force balance, and topology of Earth's magnetopause. *Science*, *356*(6341), 960–963. https://doi.org/10.1126/science.aag3112

Scholer, M. (1988), Magnetic flux transfer at the magnetopause based on single X line bursty reconnection. *Geophysical Research Letters*, *15*(4), 291–294. https://doi.org/10.1029/gl015i004p00291

Southwood, D. J., Farrugia, C. J., & Saunders, M. A. (1988), What are flux transfer events? *Planetary and Space Science*, *36*(5), 503–508. https://doi.org/10.1016/0032-0633(88)90109-2

Tan, B., Lin, Y., Perez, J. D., & Wang, X. Y. (2011), Global-scale hybrid simulation of dayside magnetic reconnection under southward IMF: Structure and evolution of reconnection. *Journal of Geophysical Research: Space Physics (1978–2012)*, *116*(A2), n/a-n/a. https://doi.org/10.1029/2010ja015580

Zhao, C. (2019). Statistical Study on Two Types Of Flux Transfer Events Observed By MMS Spacecraft. UCLA. ProQuest ID: Zhao_ucla_0031D_17883. Merritt ID: ark:/13030/m5zd31z9. Retrieved from https://escholarship.org/uc/item/5jb369td